Electric-field-induced structure and domain texture evolution in $PbZrO_3$-based antiferroelectric by *in-situ* high-energy synchrotron X-ray diffraction

Hui Liu,[1] Longlong Fan,[1] Shengdong Sun,[1] Kun Lin,[1] Yang Ren,[3] Xiaoli Tan,[2] Xianran Xing,[1] and Jun Chen[1,*]

[1]Beijing Advanced Innovation Center for Materials Genome Engineering, and School of Mathematics and Physics, University of Science and Technology Beijing, Beijing 100083, China

[2]Department of Materials Science and Engineering, Iowa State University, Ames, Iowa 50011, USA

[3]X-Ray Science Division, Advanced Photon Source, Argonne National Laboratory, Argonne, Illinois 60439, USA

*Corresponding author. junchen@ustb.edu.cn

Abstract

Antiferroelectrics (AFEs) have a great potential for modern electronic devices by virtue of the large strain during the antiferroelectric-to-ferroelectric (AFE-FE) phase transition under external electric fields. Although the fascinating macroscopic properties of AFE materials have been extensively studied, it is still unclear how the underlying structure evolution engenders their defining properties. Here we employ an electric biasing *in-situ* high-energy synchrotron X-ray diffraction technique to reveal the phase, domain texture, and lattice evolution in a high performance $PbZrO_3$-based AFE material. During the reversible AFE-FE transition triggered by electric fields, the evolution of the superstructure for AFE pseudo-tetragonal and FE rhombohedral phase is found to display strong dependence on the angle with respect to the field direction. In contrast to previous prediction, it is found that there is no obvious domain reorientation in the AFE phase, when the system is far away from the AFE-FE transitions. The electric-field-induced FE rhombohedral phase exhibits an unusual microscopic behavior, distinguished from the normal one, presenting small changes in domain texture and lattice strain with electric field, and leading to a small piezoelectric response. The longitudinal, transverse, and volume strains estimated from the XRD peak profiles are well consistent with the macroscopic strain measurements. It is demonstrated that the large strain arises from the structural change associated with anisotropic lattice strain and highly preferential domain reorientation during the AFE-FE transitions. The AFE-FE switching sequence is constructed based on the present study, which provides a further understating of AFE materials.

Keywords: Antiferroelectric ceramic; Strain; Phase transition; *In-situ* X-ray diffraction.

1. Introduction

Antiferroelectrics (AFEs) have attracted increasing attention due to their potential for important applications such as energy storage and harvesting, actuators, electrocaloric cooling devices [1-10]. The functionality of AFEs arises from a reversible transition between antiparallel and parallel dipole states under an externally applied electric field, so-called electric-field-induced AFE-to-FE transition, a process involving large macroscopic strain and polarization development [11-14]. The defining properties of these AEFs are strongly dependent on details of phase transition [5-7,15,16]. Therefore, understanding the transition in detail is a prerequisite for optimizing the design of high-performance AEFs, for instance achieving giant strains at low electric field regime and reducing hysteresis of switching electric field.

The most widely investigated AFEs are $PbZrO_3$-based perovskites [15-22]. For the prototype AFE of $PbZrO_3$, the extremely high critical electric field for the AFE-to-FE phase transition is required in the polycrystalline ceramics, which prevents the potential applications. The ternary system of $PbZrO_3$-$PbTiO_3$-$PbSnO_3$ has been developed to have sustainable critical electric field [15,16]. In these materials, the electric-field-induced AFE-to-FE transition has been extensively studied through macroscopic polarization, strain, and dielectric measurements [6,15,17,18]. It is believed that the AFE-FE structural transformation is accompanied by large volume expansion, and thus involves positive transverse and longitudinal strains [16,22]. Although a complicated incommensurate modulation structure has been observed in the various high performance $PbZrO_3$-based AFEs [19-21], the prominent structure is based on perovskite primitive unit cell with pseudo-tetragonal or orthorhombic distortion [22,27]. The structure of electric-field-induced FE phase is considered to be the rhombohedral $R3c$ symmetry [22,23]. Different types of oxygen octahedral tilting have been also found both in AFE and FE phases [16,24,25]. The AFE-FE transition is much complicated due to the interaction between AFE/FE domain reorientation, lattice, and structure change. The recovery and destruction of AFE state have been observed by *in-situ* transmission electron microscopy (TEM) studies [19,26]. The X-ray and neutron diffraction studies have indicated the changes in preferred orientation of domains during the AFE-to-FE transition [25,27,28]. In particular, Park *et al* have proposed a possible microstructural scenario of the AFE-FE switching sequence [22]. However, a detailed picture between the structural evolution and their defining properties is still missing.

Interestingly, *in-situ* high-energy synchrotron X-ray diffraction (SXRD) combined with 2D detector technology has been demonstrated to be an exceptionally powerful tool for directly monitoring and quantifying the structural evolution of FEs/AFEs under an external electric field [29-34]. The technique benefits from the strong penetrating capability of high-energy synchrotron X-rays and the resulting ability to conduct experiments in transmission geometry, thereby avoiding the notorious surface layer effects [35], and thus enabling to reveal the intrinsic response of lattice and phase transition to external electric fields. Owing to the high signal to noise ratio and high flux, the high-energy SXRD can probe the weak but very informative superstructure reflections which are typically related to AFEs. Note that the weak superstructure reflections are virtually impossible to observe with conventional XRD [17]. Furthermore, the 2D detector can simultaneously provide orientation-dependent information for anisotropic behaviors. Altogether, the technique enables the connection of the macroscopic properties with domain texture, lattice strain, and crystal symmetry change during the electric field-induced AFE-FE transition.

Herein, we report the results of *in-situ* high-energy SXRD study on the evolution of the phase, domain texture, and lattice strain in one of the most representative perovskite AFEs – Nb doped $PbZrO_3$-$PbTiO_3$-$PbSnO_3$ ternary system, in particular $Pb_{0.99}\{Nb_{0.02}[(Zr_{0.57}Sn_{0.43})_{0.94}Ti_{0.06}]_{0.98}\}O_3$ (PNZST) composition [17]. We find evidences for the presence of strong correlation between superstructure evolution and polarization development in PNZST. Markedly, we are able to estimate electric-field-induced strains through a quantitative analysis of the XRD peak profiles. The unique strains arise from the structural change associated anisotropic lattice strain and strong preferential domain reorientation during the AFE-FE phase transitions. According to the present results, we propose the AFE-FE switching sequence, which is different from the previous prediction. The results will help the development of AFE materials.

2. Experimental Section

The PNZST ceramic was fabricated by the solid-state reaction method. Analytic reagent grade PbO, Nb_2O_5, ZrO_2, SnO_2, and TiO_2 powders were used as raw materials. The homogeneous mixed powders were calcined at 850°C for 4 h and then sintered at 1300°C for 3 h. The details of the sample preparation can be seen in the ref. [17]. The relative density of the bulk ceramics is more than

95% of theoretical density and the average grain size is about 3 μm. The $S-E$ curves and $P-E$ loops were measured on ceramic disks with a diameter of 8 mm, and thickness of 0.5 mm by using a standardized ferroelectric tester (aixACCT, TF Analyzer 1000).

For the in-situ high-energy SXRD measurements, the ceramic samples were polished, cut into rectangular bars with dimensions of 6 mm×1 mm×0.6 mm, and then annealed at 500 °C for 6 h to release stresses. Gold electrodes with a size of 6 mm×1 mm were evaporated on opposite faces of the bars. The *in-situ* high-energy SXRD measurements were conducted at the 11-ID-C beamline at the Advanced Photon Source (APS) at the Argonne National Laboratory. The X-ray beam with a spot size of 0.5 mm×0.5 mm, photon energy of about 110 keV and a wavelength of 0.11165 Å were used. A Perkin Elmer amorphous silicon 2D detector, positioned approximately 1800 mm away from the sample, was used to collect the scattered photons. The direction of the electric field was perpendicular to the X-ray beam. A triangular bipolar cycle electric field (−6 kV/mm ~ +6 kV/mm) with a step of about 0.5 kV/mm was applied to the ceramic samples. At each step, a diffraction pattern was recorded with an acquisition time of 30 s, which is equivalent to a cyclic frequency around 40 mHz. The diffraction pattern of Ceria standard was used to calibrate the detector related parameters. The Debye rings collected on the 2D detector were divided into equidistant sectors at 15°. Intensities of the X-ray diffraction peaks in the sectors were integrated using the Fit2d software. The full profile LeBail fitting of AFE phase and structure refinement of FE phase were performed on the platform of JANA2006 software [36].

3. Results and discussion

3.1. Ferroelectric polarization properties

Under applied electric field, the PNZST ceramic displays well-defined double hysteresis loops, which is a signature of AFEs (Fig. 1a). The measured critical field E_F (AFE to FE transition) and E_A (FE to AFE transition) is about 3.5 kV/mm, and 0.5 kV/mm, respectively. The maximum polarization of the FE phase is about 30 μC/cm^2. The macroscopic properties in the present study are consistent with the reported values in the literature [17]. To reveal the structural evolution of the PNZST ceramic induced by electric field, *in-situ* high-energy SXRD was employed (Fig. 1b).

3.2. Electric-field-induced structure evolution

The virgin AFE state exhibits pure perovskite structure which has a prominent pseudo-tetragonal distortion (Fig. S1). The lattice parameters are estimated to be a_T = 4.1111 Å and c_T = 4.0886 Å with a structural distortion ($1-c_T/a_T$) of 0.5% through Le-Bail fitting method, which are in good agreement with the previous studies [17,19]. The structure of the FE state is determined as rhombohedral phase ($R3c$) based on the full profile structure refinement at the 45° sector (Fig. 2), which is coincident with the previous reports [24,25]. The lattice parameters of the FE state at 6 kV/mm were calculated to be a_R = 4.1150 Å and α_R = 89.8°. The calculated volume expansion is as high as 0.68%. The detailed structure evolution will be discussed later.

A characteristic feature of AEFs is the intrinsic antiparallel atomic displacement, which manifests itself as a relatively weak but clearly discernible superstructure reflections in the respective diffraction patterns. Therefore, directly monitoring these superstructure reflections can help to understand the polarization development as revealed in the double *P-E* hysteresis loops. The evolution of the superstructure reflections parallel to the direction of the applied electric field (φ = 0°) is shown in Fig. 3. At the virgin AFE state, the superstructure $\frac{1}{2}(311)_p$ and $\frac{1}{2}(331)_p$ reflections are observed beside the strong main Bragg reflections ($\boldsymbol{Q}_p$). The reflections belong to $\boldsymbol{Q}_p\pm\frac{1}{2}(111)_p$-type superstructure reflections which should be attributed to the octahedral tilting [16,37,38]. It is worth mention that these type superstructure reflections are also observed in the prototype AFE of $PbZrO_3$, which is assigned as $a^-a^-c^0$ octahedral tilting [39]. In addition, other superstructure reflections, marked with asterisks, are also seen. These indicate the presence of the incommensurate modulation which corresponds to a modulation vector $\boldsymbol{q} = {}^1/_n(110)_p^*$ (n is about 7.8). Such incommensurate superstructure reflections can be attributed to the unique modulated atomic positions and responsible for the unique polarization of AFEs [14]. The incommensurate modulation vector observed in the present study is consistent with the previous TEM study [26]. It has been suggested that such incommensurate structures result from the competing FE and AFE orderings [13,40]. With increasing electric field, no obvious change is observed in the superstructure reflections. When the field increases to 3.5 kV/mm near the shoulder of E_F, all the incommensurate superstructure reflections but the $\boldsymbol{Q}_p\pm\frac{1}{2}(111)_p$-type reflection disappears. The observation indicates the emergence of AFE to FE transition. Note that the persistent $\frac{1}{2}(311)_p$ and $\frac{1}{2}(331)_p$ superstructure reflection in the FE state is ascribed to the $a^-a^-a^-$ octahedral tilting of the rhombohedral $R3c$ phase [37], which has been confirmed by the previous TEM study [21]. Upon unloading the electric field below 0.5 kV/mm which is near the measured E_A, the incommensurate superstructure reflections reappear. These features repeat in the subsequent cycle of electric field, indicating a reversible electric field induced AFE-to-FE transition. When the intensity changes of the incommensurate superstructure reflections are compared with the double *P*-*E* hysteresis loops (Fig. 4), one can notice the existence of a strong correlation. It suggests that the electric-field-induced polarization is highly correlated with the intrinsic atomic ordering.

It is interesting to observe that the intensity of superstructure reflections for both AFE and FE exhibits strong anisotropy after exposing to electric fields (Fig. 5). Significant differences are observed in the incommensurate superstructure reflection between the virgin and the field exposed AFE state. The intensity of reflection A at the virgin state is the same over all orientations, whereas in the field-exposed sample it appears enhanced along the electric field direction (φ = 0°), while suppressed in the perpendicular direction (φ = 90°) (Fig. 5a). It implies that the initially random AFE domains develop a texture after the FE-to-AFE transition takes place. On the contrary, the ½$(311)_p$ reflections of the FE state show high intensity at φ = 90° but low intensity at φ = 0° (Fig. 5b). This scenario has also been observed in the electric-field-induced rhombohedral (*R*3*c*) phase in $(Bi_{1/2}Na_{1/2})TiO_3$-based Pb-free FEs [41,42]. It can be ascribed to strain-induced anisotropic octahedral tilting, but not to domain texturing because of no splitting of this reflection allowed.

Figures 6(a-c) show the $\{110\}_p$, $\{111\}_p$ and $\{200\}_p$ profiles, respectively, under a full cycle of bipolar electric fields at φ = 0°, 45°, and 90°. At the virgin state, the structure is confirmed to be pseudo-tetragonal symmetry as evidenced by the peak splitting of $\{200\}_p$ and the singlet $\{111\}_p$. The $(110)_p$ should split for the pseudo-tetragonal symmetry, but the diffraction resolution in the present study is insufficient to reveal. With increasing electric field, all the reflections remain largely unchanged until 3.5 kV/mm, corresponding to the measured E_F. At this critical electric field, the split $\{200\}_p$ reflections merge into singlet, suggesting the AFE to FE transition. The instantaneous peak position shift of $\{110\}_p$ is accompanied by intensity interchange of the $\{111\}_p$ reflection, which suggests an orientation dependent lattice strain and domain texture development. With further increasing electric field, FE is stable with no obvious changes in its structures. Upon decreasing the electric field to 0.5 kV/mm, the singlet $\{200\}_p$ reflection splits into doublet, and the $\{110\}_p$ and $\{111\}_p$ reflections shift back to the high angle side, indicating that the FE switches back to AFE. In contrast to the virgin AFE, the $\{200\}_p$ reflection at 0 kV/mm after the electric field exposing exhibits a strong texture. Under the subsequent cycle of applied electric field, this scenario repeats itself. It is noted that the $\{200\}_p$ reflection changes negligibly in both intensity and position for the AFE state. This suggests that the external electric field can hardly develop any domain texture in AFE. Such a reversible AFE to FE transition is in line with the observed evolution in the superstructure reflections (Fig. 3). In addition, similar evolution of the $\{210\}_p$ profile is evident (Fig. S2).

3.3. Domain texture and lattice strain analysis

It is well known that the polarization of FE rhombohedral occurs along the $[111]_p$ direction. Thus the domain texture can be evaluated from the change of the $\{111\}_p$ profile intensity [31,32]. For AFE with incommensurate modulations, the polarization is considered to lie within the $(110)_p$ plane, even though the detailed polarization configuration remains unknown. Here, the interchange of intensity of the $\{200\}_p$ profile was used to estimate the domain texture of AFE [24,25]. In order to quantify the electric-field-induced domain texture and lattice strain, the $\{111\}_p$ reflections and the $\{200\}_p$ reflections for both FE and AFE states were fitted by using with pseudo-Voigt function. The $\{111\}_p$ reflections of AFE state and the $\{200\}_p$ reflections of FE were fitted by singlet one, while doublet pseudo-Voigt shape were used to fit the $\{111\}_p$ profile of FE and the $\{200\}_p$ reflections of AFE (Fig. 7 and Fig. S3).

The domain texture can be described by the multiple random distribution (*f*) function, which is a quantitation of the degree of preferred domain orientation with respect to a random distribution [31-34]. The f_{200} of AFE and f_{111} of FE can be calculated by the following equations (1) and (2), respectively: [43]

$$f_{200} = 3 \times \frac{I^E_{200}/I^0_{200}}{2I^E_{200}/I^0_{200}+I^E_{002}/I^0_{002}} \quad (1)$$

$$f_{111} = 4 \times \frac{I^E_{111}/I^0_{111}}{I^E_{111}/I^0_{111}+3I^E_{11\bar{1}}/I^0_{11\bar{1}}} \quad (2)$$

where I^E_{hkl} is the integrated intensity of *hkl* reflection under electric field, I^0_{hkl} is the integrated intensity of *hkl* reflection at the virgin state. For FE, the ideal $I^0_{111}/I^0_{11\bar{1}}$ = 1/3 is used for the calculation. The values of f_{200} and f_{111} are identical to be 1 at the unpoled state, while 1.5 and 4 at the saturated state, respectively. According to the Bragg law, $2d_{hkl}\sin\theta = n\lambda$, the value of d_{hkl} can be obtained. The lattice strain can be calculated by:

$$\varepsilon = \frac{d_E - d_0}{d_0} \quad (3)$$

where d_E is the lattice spacing under electric field E, and d_0 is lattice spacing at the virgin state.

The value of f_{200} of AFE is shown in Fig. 8a as a function of orientation at representative electric fields. The value of f_{200} about 1.27 along electric field direction after electric field exposing, corresponds to about 85% of fully aligned domain state. The f_{200} value of AFE stays constant in the sub-critical field regime. It indicates that non-180° domain reorientation does not occur when an electric field is applied. However, the domain texture emerges in AFE during and after the electric field unloading; such a texture persists in the subsequent electric field cycles. This indicates that the domain texture in AFE is inherited from FE after the FE-to-AFE transition in the first cycle of electric field. Non-180° domain switching is not observed to occur in the subsequent cycles of electric field. In contrast, the FE state immediately exhibits a high domain texture character, once it is induced by applied field (Fig. 7b). For instance, the value of f_{111} is 3.12 at E = 6 kV/mm along the electric field direction (φ = 0°). It reaches a value 80% of the saturated state. The value is comparable to the poled rhombohedral FE state of $PbZr_{0.55}Ti_{0.45}O_3$ (PZT55, 3.48) and $0.6PbTiO_3$-$0.4BiScO_3$ (PT-40BS, 2.5) [44,45].

It is found that the value of f_{111} changes little under further applied electric fields, once the FE phase is induced. This demonstrates the character of limited non-180° domain switching in the electric-field-induced FE phase. Overall, non-180° domain reorientation hardly occurs in both AFE and FE phase, when the system is far away from the AFE-FE transition. Interestingly, a similar degree of preferred domain orientation is observed in E-exposed AFE and electric-field-induced FE phase. It suggests the inheritance between AFE and FE domains orientation. It is important to note that at the AFE-to-FE transition the switching of AFE/FE domains and the structure change occur simultaneously. The electric-field-induced FE forms with highly preferential domain orientation.

Figure 9 shows the calculated lattice strains of the characteristic $\{110\}_p$, $\{111\}_p$ profile, and $(200)_p$ reflection as a function of the bipolar electric field. Interestingly, these calculated lattice strains exhibit a shape similar to that of the measured *S-E* curves. Negligible lattice strain is observed in the virgin AFE state, while a small amount of residual strain is observed in the electric field exposed AFE (0 kV/mm). There is an abrupt change near the critical electric field which marks the AFE-to-FE transition. The change is accompanied with the emergence of orientation dependent behaviors observed in piezoelectric materials. Specifically, at E = 6 kV/mm, $\varepsilon_{(200)_p}$ is 0.06% at 0°, while it is negative, −0.02% and −0.16%, respectively, for 45° and 90° (Fig. 9a). As a comparison, the observed $\varepsilon_{(200)_p}$ at φ = 0° is much lower than the FE of PZT55 (0.20%) [44]. The corresponding piezoelectric coefficient from lattice in the electric-field-induced FE is about 110 pm/V, which is much lower than that of normal ferroelectric rhombohedral of PZT55 (330 pm/V) and PT-40BS (440 pm/V) [44,45]. It suggests that the piezoelectric response of electric-field-induced FE phase is not good. The strain of electric-field-induced FE is saturated after the AFE-FE transition. It is worth mentioning that the value of $\varepsilon_{(200)_p}$ is slightly positive at 0° but strongly negative at 90° after the AFE-to-FE transition. It is due to the change of polarization direction during the transition. On the contrary, the values of $\varepsilon_{\{110\}p}$ and $\varepsilon_{(111)p}$ are positive for all orientations. In particular, large values are observed along the applied electric field and relatively low values are observed in directions off the electric field.

3.4. Estimation of macroscopic strains

It is acknowledged that the macroscopic strain of piezoelectric materials originates from intrinsic contributions of lattice strain and structural transformation, and extrinsic contributions of domain wall motion. In the present study, although negligible domain switching is observed in both AFE and FE phase when the system is far away from the AFE-FE transition (Fig. 8), at the abrupt AFE-FE transition, the structure change is accompanied by AFE/FE domains alignment and lattice strain, both of which contribute to the macroscopic strain. The strain contribution can be estimated by the weighted-average strain of individual hkl reflection, as given by equation (4) [46].

$$S_{\varphi} = \frac{\sum_{hkl} f_{hkl}(\varphi) m_{hkl} \varepsilon_{hkl}(\varphi)}{\sum_{hkl} f_{hkl}(\varphi) m_{hkl}(\varphi)} \qquad (4)$$

where $f_{hkl}(\varphi)$ denotes the domain texture with orientation φ to the electric field, and m_{hkl} denotes the multiplicity of hkl reflections. For hkl reflections that do not have domain texture, the f_{hkl} value is 1. In this study, the characteristic $\{200\}_p$, $\{110\}_p$, and $\{111\}_p$ profiles are used for the estimation. This strategy was used in the previous studies on piezoceramics [47,48]. It is noteworthy that the strains calculated by this method unable to distinguish the individual contributions of lattice strain and domain switching, while it can offer the information for strain anisotropy. The calculated strain corresponds to the longitudinal strain (S_{33}) at $\varphi = 0°$, and to the transverse strain (S_{11}) at $\varphi = 90°$. The volume strain (S_V) is calculated as $S_{33}+2S_{11}$.

Figure 10 presents a comparison between the calculated and measured strains as a function of applied bipolar electric field. Intriguingly, there are very good agreements between the calculated lattice strains and the measured ones for the longitudinal, transverse, and volume strains. The calculated strain abruptly increases at E = 3.5 kV/mm during electric field loading, and abruptly drops at E = 0.5 kV/mm during unloading process. These critical fields correspond to the E_F and E_A measured by the macroscopic S-E curves, respectively. The calculated S_{33} and S_{11} at E = 6 kV/mm is 0.30%, and 0.073%, respectively, which both approximate the measured ones (x_{33} = 0.28, x_{11} = 0.070%). It needs to note that the measured negative transverse x_{11} (about −0.02%) during the second cycle of applied electric fields can be also reproduced by the quantification (S_{11} = −0.021%). In addition, the calculated volume strain S_V at E = 6 kV/mm is 0.45 %, which is slightly higher than the measured one (0.42 %). The electric-field-induced FE rhombohedral phase presents an unusual microscopic behavior of small changes in domain texture and lattice strain with electric field, and results in a small piezoelectric response. It would be attributed to the unique domain configuration after the AFE-to-FE transition [49-51]. The existence of antiphase-type oxygen octahedral tilting in the electric-field-induced FE rhombohedral phase can lead to antiphase boundary, which suppresses the domain walls motion, and reduces the extrinsic contributions to the piezoelectric response [52]. Besides, such small piezoelectric response would be due to the saturation of electric-field-induced strain in high field regime. Compared with piezoelectric materials, the large strain in AFE stems from structural phase transition, which generates large anisotropic lattice strain and highly preferential domain reorientation.

Based on the results revealed in the present *in-situ* study, a revised AFE-FE switching sequence is presented in Fig. 11. The randomly oriented AFEs at the virgin state remains under applied electric field. This scenario is is consistent with a recent observation [25], but different with the previous assumption [22], in which the randomly oriented AFE is forced to orient preferentially. When the electric field reaches E_F, the randomly oriented AFE phase switches into highly oriented domain in FE phase. After that, the sample cannot resume its virgin state. At critical electric field, the AFE pseudo-tetragonal structure change to FE rhombohedral structure, associated with large anisotropic lattice strain and highly preferential domain reorientation, and results in positive transverse and longitudinal macroscopic strains. In contrast to previous prediction [22], it is found that, when the applied electric field beyond the critical electric field, the domain texture and the lattice strains change little with electric field in the electric-field-induced FE phase, and leading to an unusually small piezoelectric response in comparison with normal ferroelectric rhombohedral phase. When the electric field is removed, the metastable FE transforms back into AFE with a preferentially domain orientation inherited from FE phase. While in the subsequent cycle electric field, no further changes of AFE domain texture happen.

$PbZrO_3$-based AFE materials exhibit a similar electric-field-induced macroscopic behavior of double *P*-*E* loops, such as La or Nb doped $PbZrO_3$-$PbTiO_3$-$PbSnO_3$ ternary systems [15,16]. It is reasonable to believe that the microstructural evolution during the AFE/FE phases of the present study is general for the $PbZrO_3$-based AFE materials. It is well known that both critical electric field of the AFE-to-FE transition and the electric-field-induced strain are important properties for practical applications. Previous studies have demonstrated that the critical electric field can be modified by introducing strong ferroelectricity activity cation of Ti^{4+} to weaken antiferroelectric ordering in $PbZrO_3$, and incommensurate modulated structures emerge [17,21], and the AFE phase presents much smaller structure distortion (0.5%) in comparison with $PbZrO_3$ (1.3%). Those are some of the structure reasons for the reduced critical electric field. On the other hand, the anisotropic lattice strains and domain reorientations at the AFE-FE transition are important for the longitudinal strain. Increasing the anisotropy of both factors would enhance the desired longitudinal strain at the expense of the transverse strain, such as controlling grain orientation.

4. Conclusions

In summary, the detailed picture of the phase evolution correlating with strain and polarization development is elucidated for a typical $PbZrO_3$-based AFE ceramic using *in-situ* high-energy SXRD. Structural data demonstrate the presence of anisotropic superstructure evolution during electric-field-induced reversible AFE-FE transition. No obvious domain reorientation in AFE phase is observed when the system is far away from AFE-FE transition. The electric-field-induced FE rhombohedral phase exhibits small changes in both domain texture and lattice strain with electric field, and leading to an unusually small piezoelectric response. The excellent agreement between measured and computed strains demonstrates that the large macroscopic strain stems from intrinsic structural change associated anisotropic lattice strain and highly preferential domain reorientation at the AFE-FE transitions. These results provide a clear microstructural description of the material response to applied electric fields, and are helpful for the development of new AFE materials for applications in actuators and electrocaloric cooling devices.

Acknowledgements

This work was supported by the National Natural Science Foundation of China (Grant Nos. 21825102, 21731001, and 21590793), and the Fundamental Research Funds for the Central Universities, China (Grant No. FRF-TP-18-001C2). H. L. thanks the financial support from China Scholarship Council and X.T. acknowledges the financial support by the U.S. National Science Foundation (NSF) through Grant DMR-1700014. This research used resources of the Advanced Photon Source, a U.S. Department of Energy (DOE) Office of Science User Facility operated for the DOE Office of Science by Argonne National Laboratory under Contract No. DE-AC02-06CH11357.

References

[1] A.S. Mischenko, Q. Zhang, J.F. Scott, R.W. Whatmore, N.D. Mathur, Giant electrocaloric effect in thin-film $PbZr_{0.95}Ti_{0.05}O_3$, Science 311 (2006) 1270-1271.

[2] B. Xu, J. Íñiguez, L. Bellaiche, Designing lead-free antiferroelectrics for energy storage, Nat. Commun. 8 (2017), 15682.

[3] J. Li, F. Li, Z. Xu, S. Zhang, Multilayer lead-free ceramic capacitors with ultrahigh energy density and efficiency, Adv. Mater. 30 (2018), 1802155.

[4] L. Yang, X. Kong, F. Li, H. Hao, Z. Cheng, H. Liu, J. Li, S. Zhang, Perovskite lead-free dielectrics for energy storage applications, Prog. Mater. Sci. 102 (2019) 72-108.

[5] L. Zhao, Q. Liu, J. Gao, S. Zhang, J. Li, Lead-free antiferroelectric silver niobate tantalate with high energy storage performance, Adv. Mater. 29 (2017), 1701824.

[6] F. Zhuo, Q. Li, Y. Zhou, Y. Ji, Q. Yan, Y. Zhang, W. Cao, Large field-induced strain, giant strain memory effect, and high thermal stability energy storage in $(Pb,La)(Zr,Sn,Ti)O_3$ antiferroelectric single crystal, Acta Mater. 148 (2018) 28-37.

[7] A. Pérez-Tomás, M. Lira-Cantú, G. Catalan, Above-bandgap photovoltages in antiferroelectrics, Adv. Mater. 28 (2016) 9644-9647.

[8] S. Zhang, A.B. Kounga, W. Jo, C. Jamin, K. Seifert, T. Granzow, J. Rödel, D. Damjanovic, High-strain lead free antiferroelectric electrostrictors, Adv. Mater 21 (2009) 4716-4720.

[9] P. Gao, Z.H. Liu, N. Zhang, H. Wu, A.A. Bokov, W. Ren, Z.G. Ye, New antiferro-electric perovskite system with ultrahigh energy-storage performance at low electric field, Chem. Mater. 31 (2018) 979-990.

[10] R.Z. Zuo, J. Fu, H. Qi, Stable antiferroelectricity with incompletely reversible phase transition and low volume-strain contribution in $BaZrO_3$ and $CaZrO_3$ substituted $NaNbO_3$ ceramics, Acta Mater. 161 (2018) 352-359.

[11] C. Kittel, Theory of antiferroelectric crystals, Phys. Rev. 82 (1951) 729-732.

[12] E. Sawaguchi, H. Maniwa, S. Hoshino, Antiferroelectric structure of lead zirconate, Phys. Rev. (83) 1951, 1078.

[13] A.K. Tagantsev, K. Vaideeswaran, S.B. Vakhrushev, A.V. Filimonov, R.G.Burkovsky, A. Shaganov, D. Andronikova, A.I. Rudskoy, A.Q.R. Baron, H.Uchiyama, D. Chernyshov, A. Bosak, Z. Ujma, K. Roleder, A. Majchrowski, J.H. Ko, N. Setter, The origin of antiferroelectricity in $PbZrO_3$, Nat. Commun. 4 (2013), 2229.

[14] I. MacLaren, R. Villaurrutia, B. Schaffer, L. Houben, A. Pelaiz-Barranco, Atomic-scale imaging and quantification of electrical polarisation in incommensurate antiferroelectric lanthanum-doped lead zirconate titanate, Adv. Funct. Mater. 22 (2012) 261-266.

[15] X. Hao, J.W. Zhai, L.B. Kong, Z.K. Xu, A comprehensive review on the progress of lead zirconate-based antiferroelectric materials, Prog. Mater. Sci. 63 (2014) 1-57.

[16] X. Tan, C. Ma, J. Frederick, S. Beckman, K.G. Webber, The antiferroelectric↔ferroelectric phase transition in lead-containing and lead-free perovskite ceramics, J. Am. Ceram. Soc. 94 (2011) 4091-4107.

[17] J. Frederick, X. Tan, W. Jo, Strains and polarization during antiferroelectric-ferroelectric phase switching in $Pb_{0.99}Nb_{0.02}((Zr_{0.57}Sn_{0.43})_{1-y}Ti_y)_{0.98}O_3$ ceramics, J. Am. Ceram. Soc. 94 (2011) 1149-1155.

[18] F. Zhuo, Q. Li, J.H. Gao, Q. Yan, Y. Zhang, X. Xi, X. Chu, Phase transformations, anisotropic pyroelectric energy harvesting and electrocaloric properties of $(Pb,La)(Zr,Sn,Ti)O_3$ single crystals, Phys. Chem. Chem. Phys. 19 (2017) 13534-13546.

[19] H. He, X. Tan, Electric-field-induced transformation of incommensurate modulations in antiferroelectric $Pb_{0.99}Nb_{0.02}((Zr_{1-x}Sn_x)_{1-y}Ti_y)_{0.98}O_3$, Phys. Rev. B 72 (2005), 024102.

[20] Z. Xu, X. Dai, Viehland, D. Impurity-induced incommensuration in antiferroelectric La-modified lead zirconate titanate, Phys. Rev. B 51 (1995), 6261.

[21] D. Viehland, D. Forst, Z. Xu, J.F. Li, Incommensurately modulated polar structures in antiferroelectric Sn-modified lead zirconate titanate: the modulated structure and its influences on electrically induced polarizations and strains, J. Am. Ceram. Soc. 78 (1995), 2101.

[22] S.E. Park, M.J. Pan, K. Markowski, S. Yoshikaw, and L.E. Cross, Electric field induced phase transition of antiferroelectric lead lanthanum zirconate titanate stannate ceramics, J. Appl. Phys. 82 (1997) 1798-1803.
[23] C.T. Blue, J.C. Hicks, S.E. Park, S. Yoshikawa, L.E. Cross, *In situ* x-ray diffraction study of the antiferroelectric-ferroelectric phase transition in PLSnZT, Appl. Phys. Lett. 68 (1996), 2942-2944.
[24] T. Lu, A.J. Studer, D. Yu, R.L. Withers, Y. Feng, H. Chen, S.S. Islam, Z. Xu, Y. Liu, Critical role of the coupling between the octahedral rotation and A-site ionic displacements in $PbZrO_3$-based antiferroelectric materials investigated by in situ neutron diffraction, Phys. Rev. B 96 (2017), 214108.
[25] T. Lu, A.J. Studer, L. Noren, W. Hu, D. Yu, B. McBride, Y. Feng, R.L. Withers, H. Chen, Z. Xu, Y. Liu, Electric-field-induced AFE-FE transitions and associated strain/preferred orientation in antiferroelectric PLZST, Sci. Rep. 6 (2015) 23659.
[26] H. Guo, X. Tan, Direct observation of the recovery of an antiferroelectric phase during polarization reversal of an induced ferroelectric phase, Phys. Rev. B 91 (2015), 144104.
[27] X. Tan, J. Frederick, C. Ma, W. Jo, J. Rödel, Can an electric field induce an antiferroelectric phase out of a ferroelectric phase? Phys. Rev. Lett. 105 (2010) 255702.
[28] I.V. Ciuchi, C.C. Chung, C.M. Fancher, J. Guerrier, J.S. Forrester, J.L Jones, C. Galassi, Field-induced antiferroelectric to ferroelectric transitions in $(Pb_{1-x}La_x)(Zr_{0.90}Ti_{0.10})_{1-x}O_3$ investigated by in situ X-ray diffraction, J. Eur. Ceram. Soc. 37 (2017) 4631-4636.
[29] H. Liu, J. Chen, L. Fan, Y. Ren, Z. Pan, K.V. Lalitha, J. Rödel, X. Xing, Critical role of monoclinic polarization rotation in high-performance perovskite piezoelectric materials, Phys. Rev. Lett. 119 (2017), 017601.
[30] H. Liu, J. Chen, H. Huang, L. Fan, Y. Ren, Z. Pan, J. Deng, L.Q. Chen, X. Xing, Role of reversible phase transformation for strong piezoelectric performance at the morhpotropic phase boundary, Phys. Rev. Lett. 120 (2018), 055501.
[31] Y. Li, Y. Chen, Z. Zhang, A. Kleppe, D.A. Hall, *In-situ* XRD study of actuation mechanisms in $BiFeO_3$-$K_{0.5}Bi_{0.5}TiO_3$-$PbTiO_3$ ceramics, Acta Mater. 168 (2019) 411-425.
[32] A. Pramanick, D. Damjanovic, J.E. Daniels, J.C. Nino, J.L. Jones, Origins of electro-mechanical coupling in polycrystalline ferroelectrics during subcoercive electrical loading, J. Am. Ceram. Soc. 94 (2011) 293-309.
[33] M. Hinterstein, M. Hoelzel, J. Rouquette, J. Haines, J. Glaum, H. Kungl, M. Hoffman, Interplay of strain mechanisms in morphotropic piezoceramics, Acta Mater. 94 (2015) 319-327.
[34] J. Schultheiß, L. Liu, H. Kungl, M. Weber, L.K. Venkataraman, S. Checchia, D. Damjanovic,

J.E. Daniels, J. Koruza, Revealing the sequence of switching mechanisms in polycrystalline ferroelectric/ferroelastic materials, Acta Mater. 157 (2018) 355-363.
[35] T. Lu, A.J. Studer, D. Cortie, K. Lau, D. Yu, Y. Feng, H. Chen, Z. Xu, R.L. Withers, G.J. McIntyre, Y. Liu, Susceptible ferroelectric/antiferroelectric phase transition near the surface of Nb-doped lead zirconate stannate titanate from surface processing, ACS Appl. Mater. Interf. 8 (2016) 14313-14317.
[36] V. Petricek, M. Dusek, L. Palatinus, Crystallographic computing system JANA2006: general features, Z. Kristallogr. 229 (2014) 345.
[37] A.M. Glazer, The classification of tilted octahedra in perovskites, Acta Crystallogr, Sect. B 28 (1972), 3384.
[38] A.M. Glazer, Simple ways of determining perovskite structures, Acta Cryst. Sect. A 31 (1975) 756-762.
[39] D.L. Corker, A.M. Glazer, J. Dec, K. Roleder, R.W. Whatmore, a re-investigation of the crystal structure of the perovskite $PbZrO_3$ by X-ray and neutron diffraction, Acta Cryst. Sect. B 53 (1997) 135.
[40] E.V. Balashova, A.K. Tagantsev, Polarization response of crystals with structural and ferroelectric instabilities, Phys. Rev. B 48 (1993), 9979.
[41] H. Simons, J. Daniels, W. Jo, R. Dittmer, A. Studer, M. Avdeev, J. Rödel, M. Hoffman, Electric-field-induced strain mechanisms in lead-free 94%$(Bi_{1/2}Na_{1/2})TiO_3$-6%$BaTiO_3$, Appl. Phys. Lett. (98) 2011, 082901.
[42] M. Acosta, L.A. Schmitt, C. Cazorla, A. Studer, A. Zintler, J. Glaum, H.J. Kleebe, W. Donner, M. Hoffman, J. Rödel, M. Hinterstein, Piezoelectricity and rotostriction through polar and non-polar coupled instabilities in bismuth-based piezoceramics, Sci. Rep. 6 (2016) 28742.
[43] J.L. Jones, E.B. Slamovich, K.J. Bowman, Domain texture distributions in tetragonal lead zirconate titanate by x-ray and neutron diffraction, J. Appl. Phys. 97 (2005) 034113.
[44] L. Fan, J. Chen, Y. Ren, X. Xing, Structural correlation to piezoelectric and ferroelectric mechanisms in rhombohedral $Pb(Zr,Ti)O_3$ ceramics by *in-situ* synchrotron diffraction, Inorg. Chem. (57) 2018 3002-3007.
[45] K.V. Lalitha, C.M. Fancher, J.L. Jones, R. Ranjan, Field induced domain switching as the origin of anomalous lattice strain along non-polar direction in rhombohedral $BiScO_3$-$PbTiO_3$ close to the morphotropic phase boundary, Appl. Phys. Lett. 107 (2015) 052901.
[46] M.R. Daymond, The determination of a continuum mechanics equivalent elastic strain from the analysis of multiple diffraction peaks, J. Appl. Phys. 96 (2004) 4263-4272.

[47] C. Zhao, D. Hou, C.-C. Chung, H. Zhou, A. Kynast, E. Hennig, W. Liu, S. Li, J.L. Jones, Deconvolved intrinsic and extrinsic contributions to electrostrain in high performance Nb-doped Pb $(Zr_xTi_{1-x})O_3$ piezoceramics ($0.50 \leq x \leq 0.56$), Acta Mater. 158 (2018) 369-380.
[48] M.C. Ehmke, N.H. Khansur, J.E. Daniels, J.E. Blendell, K.J. Bowman, Resolving structural contributions to the electric-field-induced strain in lead-free $(1-x)Ba(Zr_{0.2}Ti_{0.8})O_3-x(Ba_{0.7}Ca_{0.3})TiO_3$ piezoceramics, Acta Mater. 66 (2014) 340-348.
[49] Z. Fan, F. Xue, G. Tutuncu, L.Q. Chen, X. Tan, Interaction dynamics between ferroelectric and antiferroelectric domains in a $PbZrO_3$-based ceramic. Phy. Rev. App. 11 (2019) 064050.
[50] H. Liu, Origin of the intermediate phase in lead zirconate $PbZrO_3$. J. Am. Ceram. Soc. 101 (2018) 5281-5286.
[51] C.J. Cheng, D. Kan, S.H. Lim, W.R. McKenzie, P.R. Munroe, L.G. Salamanca-Riba, R.L. Withers, I. Takeuchi, V. Nagarajan, Structural transitions and complex domain structures across a ferroelectric-to-antiferroelectric phase boundary in epitaxial Sm-doped $BiFeO_3$ thin films. Phys. Rev. B 80 (2009) 014109.

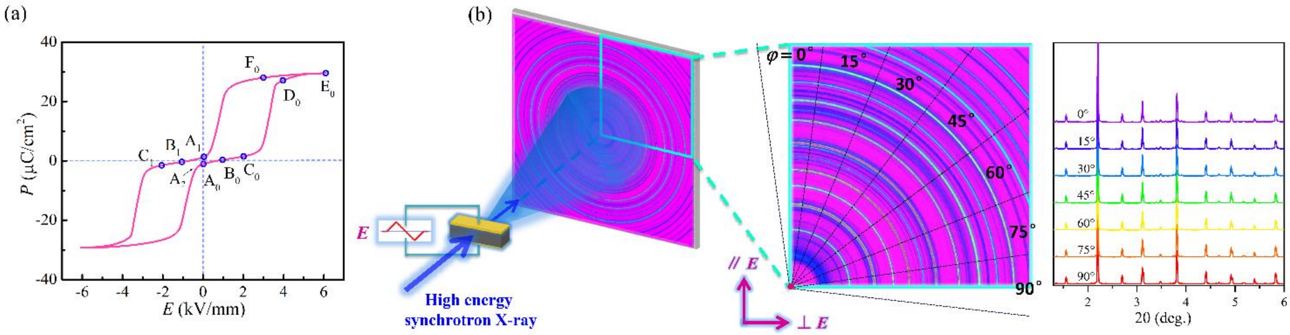

Figure 1. (a) P-E hysteresis loops of PNZST ceramics measured at room temperature at 1 Hz. The letters indicate different polarization states. (b) Schematic of the experimental setup for in-situ high-energy synchrotron X-ray diffraction experiments.

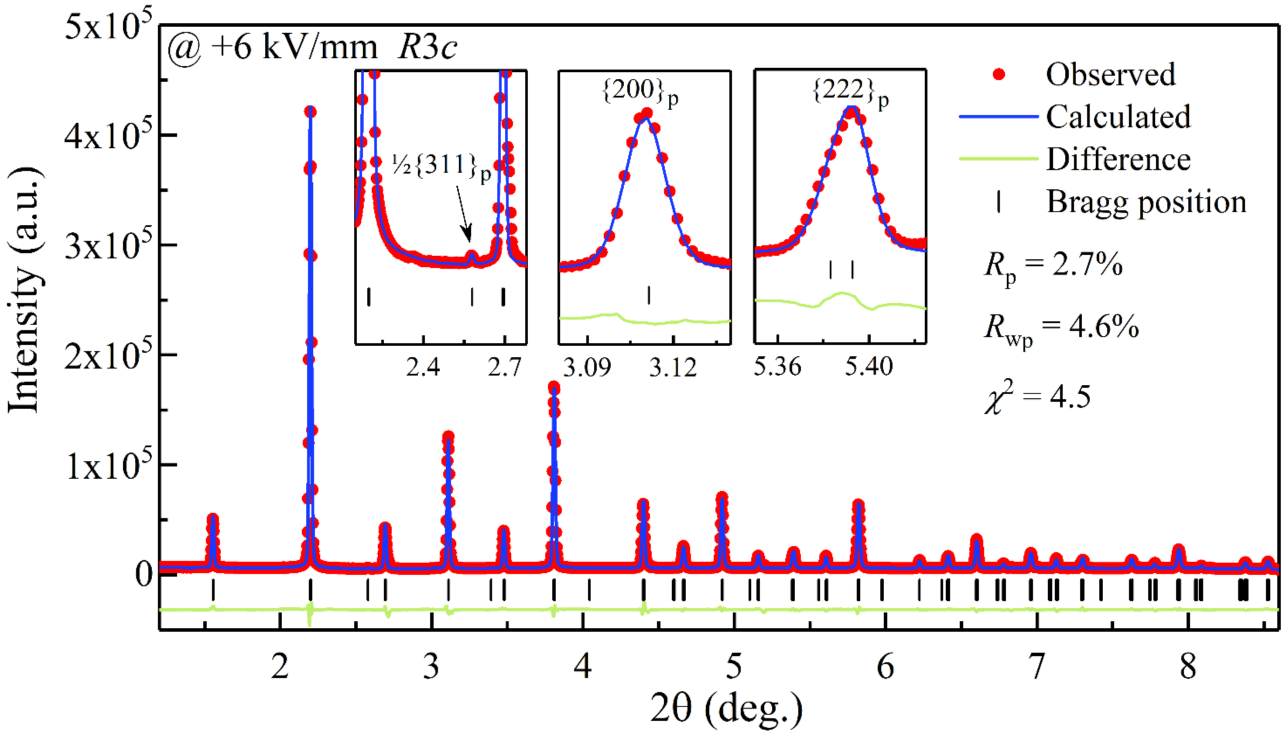

Figure 2. Full-profile Rietveld refinement of PNZST at 6 kV/mm at 45° sector. The insets show the enlarge of ½$\{311\}_p$, $\{200\}_p$ and $\{222\}_p$ profile.

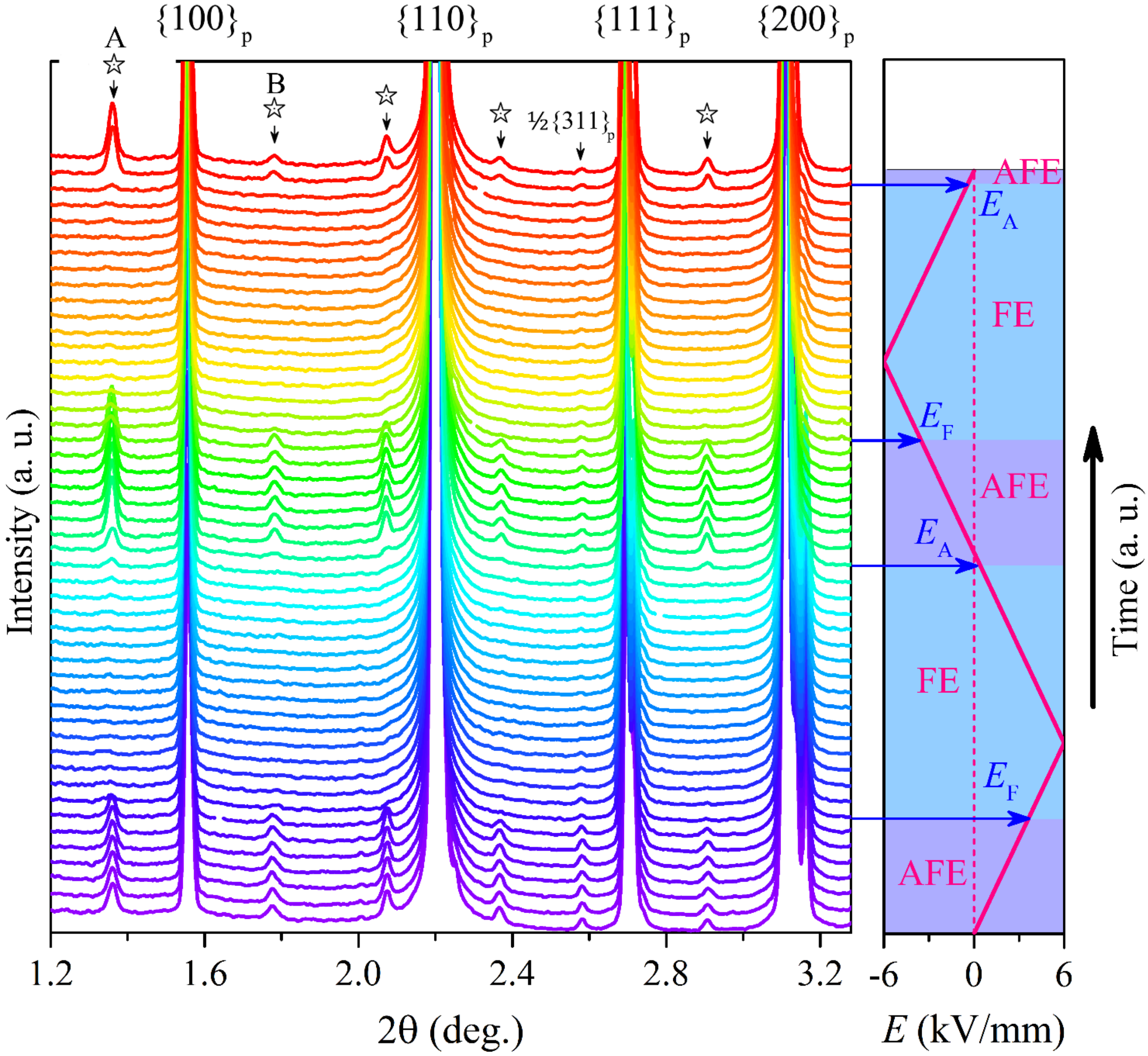

Figure 3. Evolution of satellite peaks as function of bipolar electric field at φ = 0°. The incommensurate peaks are marked with asterisks.

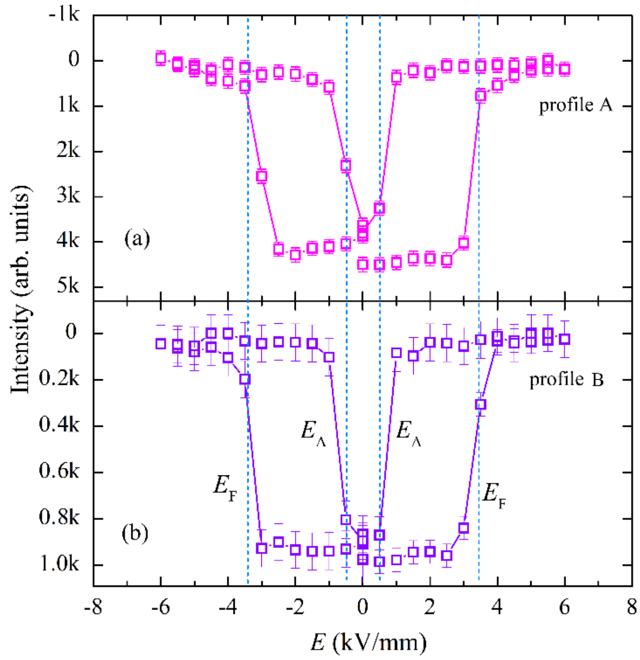

Figure 4. The integrated intensity of incommensurate profile A (a), and profile B (b) with the applied bipolar electric field.

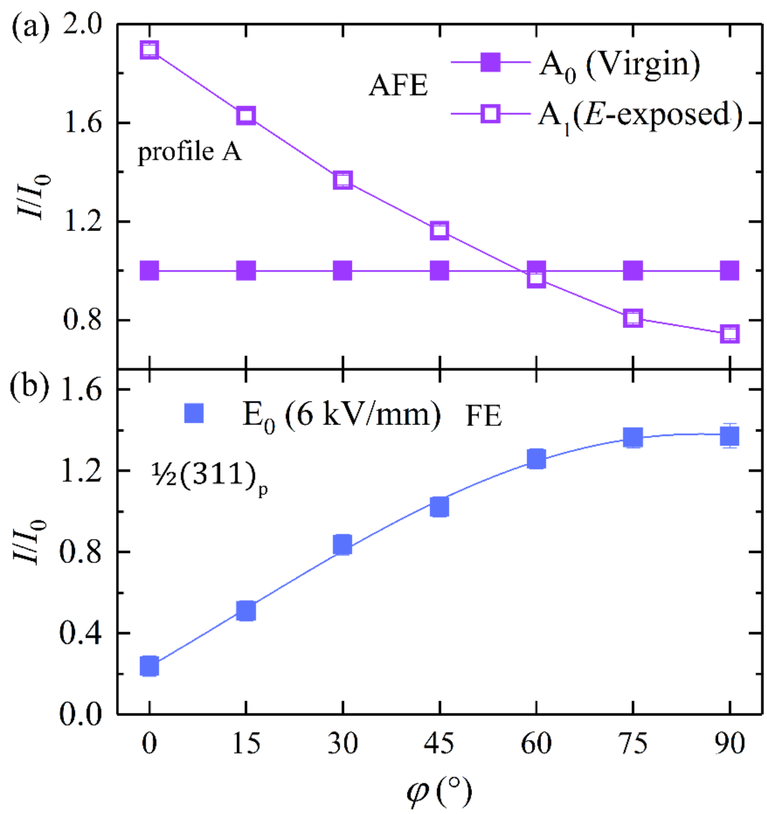

Figure 5. (a) Ratio of the integrated intensity of the superstructure profile A of AEF phase, and (b) the ½$(311)_p$ reflection of EF phase as a functions of φ at various electric field.

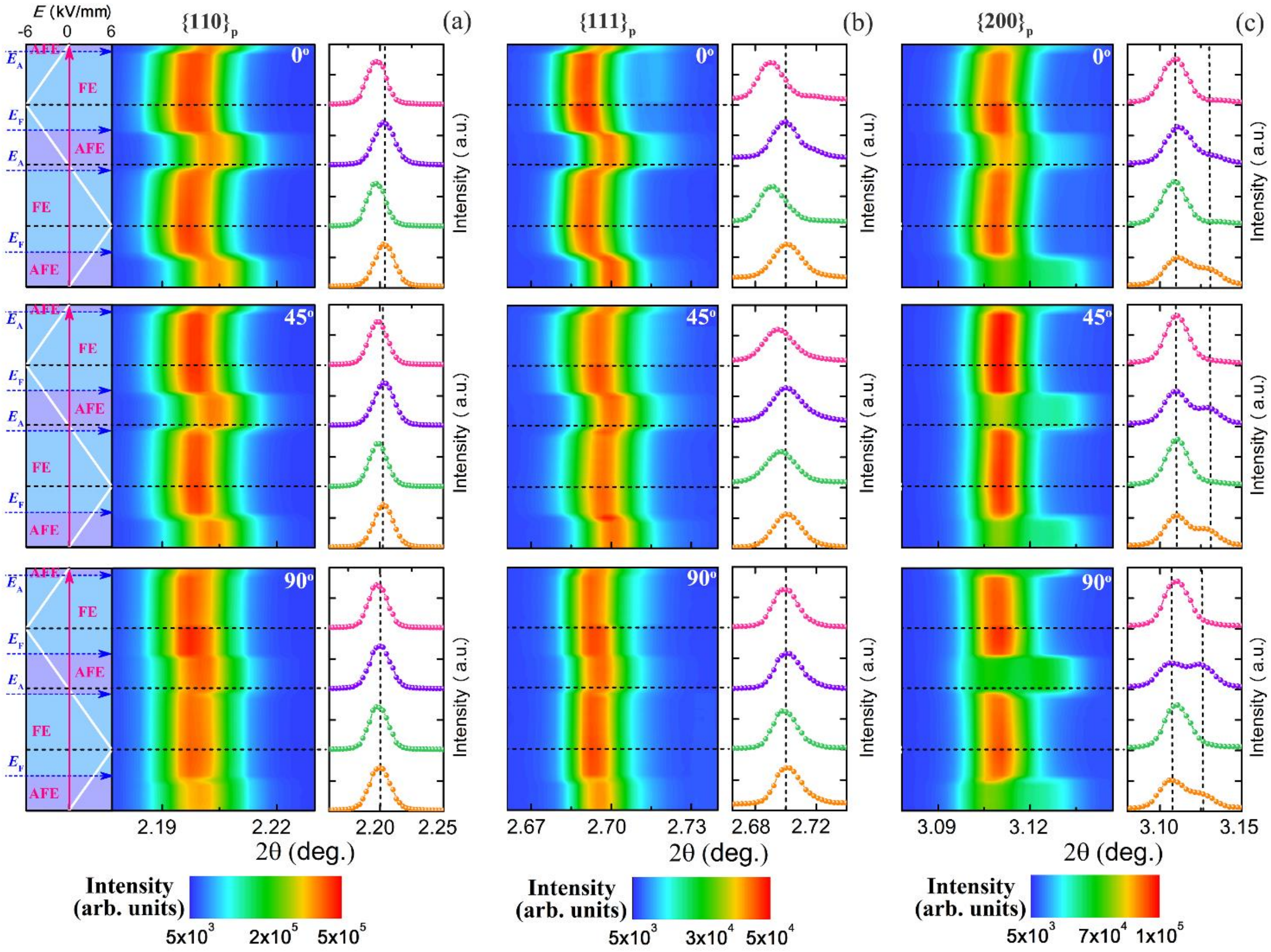

Figure 6. Contour plots of *in-situ* diffraction patterns. (a) Evolution of $(110)_p$, (b) $(111)_p$, and (c) $(200)_p$ profiles as a function of bipolar electric field at φ = 0°, 45° and 90°. The patterns on right-hand of each contour plot correspond to the profile at the virgin AFE state (yellow), positive maximum electric field of the FE state (green), electric-field exposed AFE state (purple), and at negative maximum electric field of the FE state (pink). The dashed line represents the profile center for the virgin state.

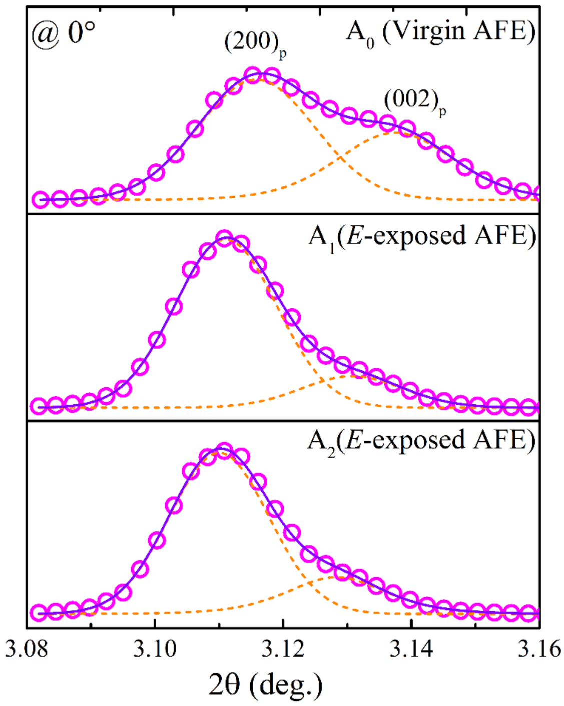

Figure 7. The fitted diffraction patterns of $\{200\}_P$ profiles for AFE state at 0° sector. The open circles, the blue solid line, and the dot line indicate the observed, the fitted, and the fitted individual peaks, respectively.

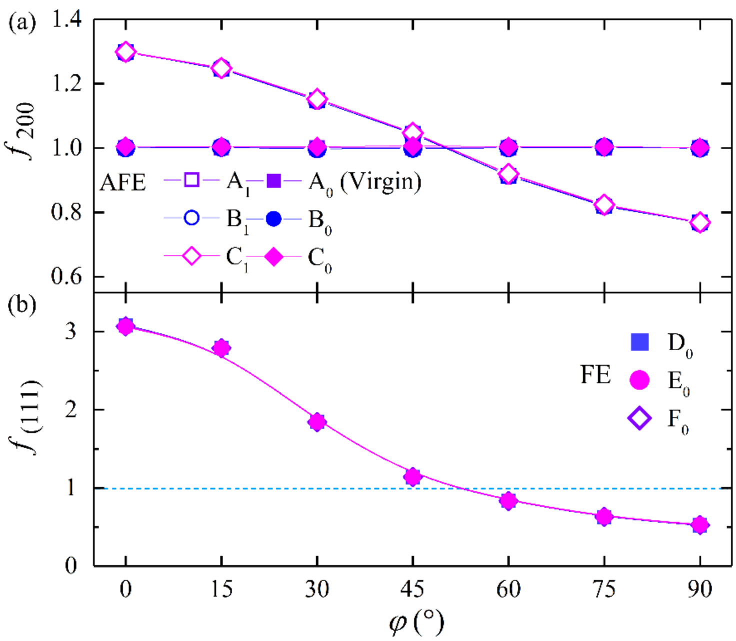

Figure 8. (a) f_{200} for the antiferroelectric phase, and (b) $f_{(111)}$ for the ferroelectric phase as a function of orientation (φ) and various electric fields. The states of electric field, indicated by letters, can be referred to Fig. 1a.

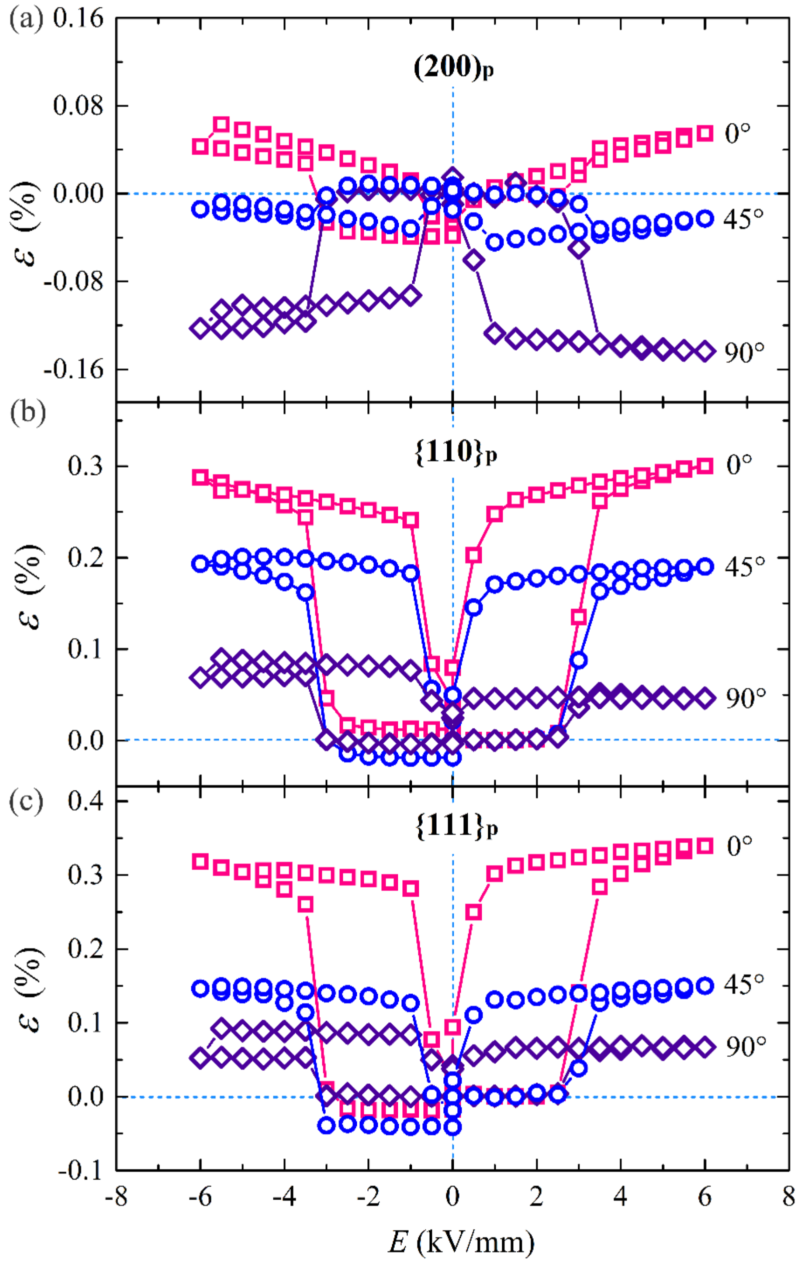

Figure 9. (a) Calculated lattice strain of (a) $(200)_p$, (b) $\{110\}_p$, and (c) $\{111\}_p$ reflections as a function of bipolar electric field.

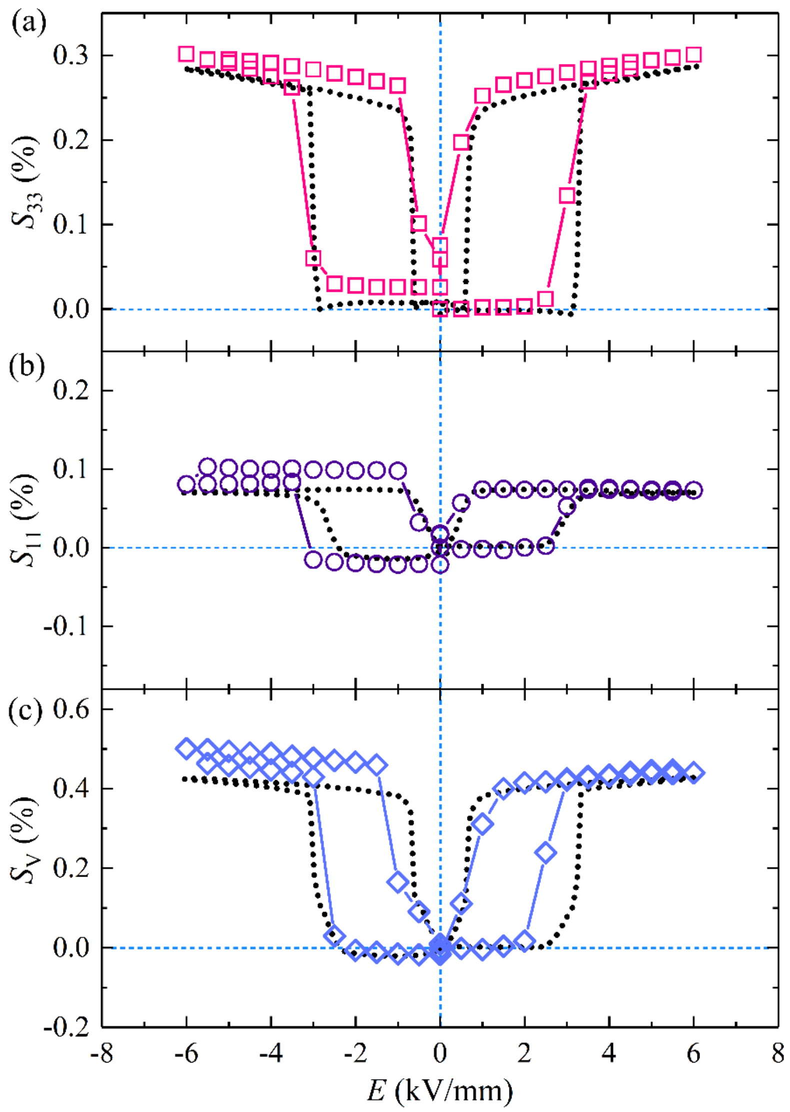

Figure 10. Comparison between the calculated (hollow point) and the macroscopic measured strains (black point) in the PNZST ceramics as a function of applied electric field: (a) longitudinal strain, (b) transverse strain, and (c) volume strain. The macroscopic measured strains are taken from Ref. [17].

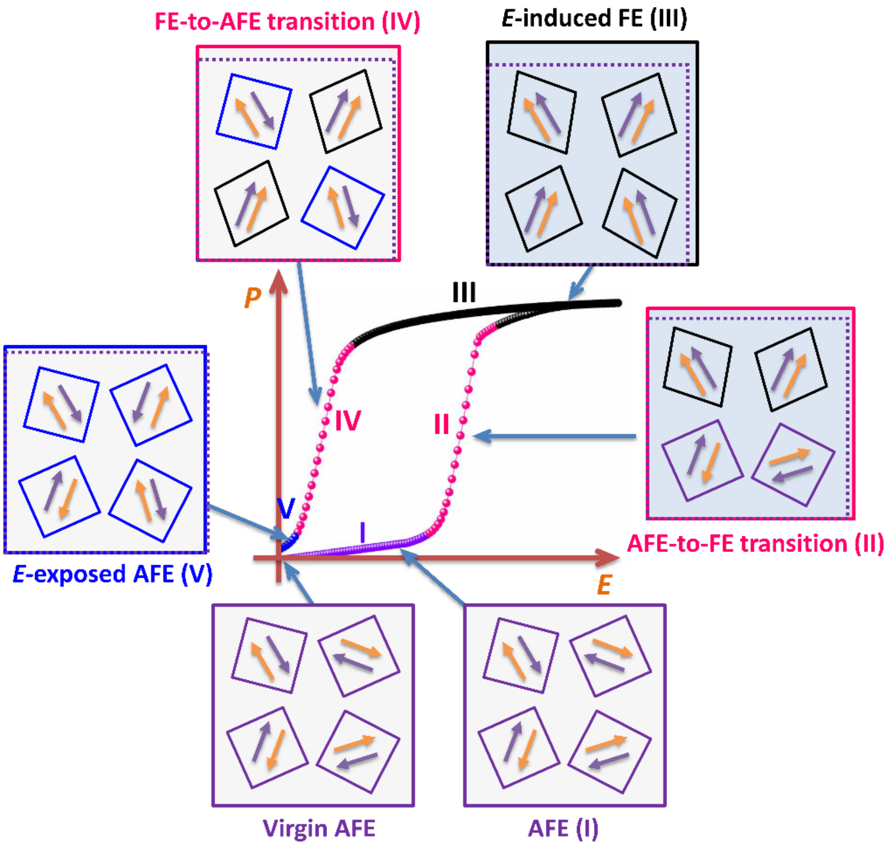

Figure 11. Simplified schematic diagram of AFE-to-FE phase switching sequence. Firstly, there is little change at the step I from the virgin AFE state. At the step II, the AFE-to-FE transition occurs. At the step III, the rhombohedral domains are highly aligned. At the step IV, some domains transformed back to AFE. At the step V, all domains transformed back to AFE but with an inherited orientation from FE.